In vivo characterization of the connectivity and subcomponents of the human globus pallidus

Patrick Beukema[1,3], Fang-Cheng Yeh[2,3], & Timothy Verstynen[2,3]

[1]Center for Neuroscience
University of Pittsburgh
Pittsburgh, PA 15260

[2]Department of Psychology
[3]Center for the Neural Basis of Cognition
Carnegie Mellon University
Pittsburgh, PA 15213

Corresponding Author:
Timothy Verstynen
Carnegie Mellon University
Department of Psychology
340 U Baker Hall
Pittsburgh, PA 15213
412-268-4615 (office phone)
timothyv@andrew.cmu.edu

Abstract

Projections from the substantia nigra and striatum traverse through the pallidum on the way to their targets. To date, in vivo characterization of these pathways remains elusive. Here we used high angular resolution diffusion imaging (N=138) to study the characteristics and structural subcompartments of the human pallidum. Our results show that the diffusion orientation distribution at the pallidum is asymmetrically oriented in a dorsolateral direction, consistent with the orientation of underlying fiber systems. Furthermore, compared to the outer pallidal segment, the internal segment has more peaks in the orientation distribution function and stronger anisotropy in the primary fiber direction, consistent with known cellular differences between the underlying nuclei. These differences in orientation, complexity, and degree of anisotropy are sufficiently robust to automatically segment the pallidal nuclei using diffusion properties. Thus the gray matter diffusion signal can be useful as an in vivo measure of the collective nigrostriatal and striatonigral pathways.

Keywords: basal ganglia, diffusion imaging, nigrostriatal, striatonigral, globus pallidus

51 **Introduction**

52 The basal ganglia are a crucial forebrain network associated with many cognitive

53 functions, including reward processing, decision-making, and learning (Hollerman et al.,

54 2000; Haber, 2003).   Many aspects of basal ganglia function rely on dopaminergic

55 inputs from the substantia nigra that serve as a modulatory signal for neurons in the

56 subpallium (Haber et al., 2000). These dopaminergic inputs are conducted by a set of

57 fiber bundles that originate in the pars compacta region of the substantia nigra, a portion

58 of which migrate in a dorsolateral direction through the segments of the globus pallidus

59 (Carpenter and Peter, 1972). While a majority of these projections pass through the

60 pallidum and terminate on cells in the striatal nuclei (Carpenter and McMasters, 1964), a

61 significant number of them also terminate in the inner and outer segments of the globus

62 pallidus, forming the nigropallidal pathway (Cossette et al., 1999). Two other major fiber

63 systems traversing through the globus pallidus project from the striatum, including the

64 striatopallidal fiber systems, which form the canonical direct and indirect pathways, and

65 the striatonigral fiber system. Breakdowns in these various pathways form the etiology

66 of several neurodegenerative diseases. For example, axonal degeneration of the

67 nigrostriatal pathway is the pathological hallmark of Parkinson's Disease (Burke and

68 O'Malley, 2013) while Huntington's disease is characterized by a loss of medium spiny

69 neurons within the striatum that project to the globus pallidus (Reiner et al., 1988). Thus

70 *in vivo* characterization of these basal ganglia projections has clear clinical implications.

71

72   One problem with characterizing both the nigral and striatal efferents is that they are

73   largely embedded within the gray matter of several basal ganglia nuclei, primarily within

74   the globus pallidus. The globus pallidus is the primary output of the basal ganglia

75   network, sending projections that relay signals from upstream nuclei to the thalamus

76   (Alexander et al., 1986). In primates it is comprised of an external segment (GPe),

77   which serves as an inhibitory relay nucleus within the indirect pathway, and the internal

78   segment (GPi) that aggregates all information from all basal ganglia pathways. While

79   primarily defined by their connectivity and neurophysiological profiles, the GPe and GPi

80   are also distinguishable at the cellular level by differences in cell density, cell type, and

81   morphology (Hardman et al., 2002, Eid et al 2013, Difiglia and Rafols, 1988). One of

82   the most salient differences is that the GPi has a much lower overall neuronal density

83   (see table 2 in Hardman et al., 2002). More importantly, given that the volume of the GPi

84   is smaller than that of the GPe and that both nigrostriatal and striatonigral fibers pass

85   through the globus pallidus on their way to their targets, the GPi also has a greater

86   density of both nigrostriatal and striatonigral efferents than its external counterpart.

87

88   Despite the clear morphological differences, in vivo characterization of these critical

89   nuclei remains elusive by MRI-based neuroimaging technologies, particularly with

90   conventional T1-weighted or T2-wighted images used in most human neuroimaging

91   experiments. This is because T1-weighted and T2-weighted approaches have limited

92   power to characterize the microscopic structure of the GPe and the GPi. This limitation

93   can be compensated by the recent advances in high angular resolution diffusion MRI,

4

94   which offers a non-invasive approach to study microscopic structure. One advantage of

95   diffusion MRI is that it is able to detect microscopic differences in underlying cellular

96   morphologies, including spatial asymmetry in underlying axonal tracts, and it has shown

97   great promise in quantifying variability in underlying tissue composition (Behrens et al.,

98   2003). With these unique features, diffusion MRI has emerged as an increasingly

99   popular tool for characterizing the neural tissues (Abhinav et al., 2014). While most

100 commonly used to study structural subcomponents of large white matter fascicles

101 (Bastiani, 2012, Wang et al, 2013, Fernandez-Miranda 2014), diffusion MRI has also

102 been shown to be useful for characterizing differences in microstructural cellular

103 properties of gray matter (Wiegell et al., 2003; Mang et al., 2012), including sensitivity to

104 both neural and glial distribution patterns (Blumenfeld-Katzir et al., 2011). For example,

105 analysis of the diffusion MRI signal has been used to segment the different thalamic

106 nuclei in humans (Behrens et al, 2003).

107

108 Here we adopt an atlas approach to study the orientation distribution functions of the

109 water diffusion, termed spin distribution functions (SDF; Yeh et al. 2010) within the gray

110 matter of the globus pallidus in a stereotaxic space. An SDF provides a nonparametric

111 representation of the diffusion pattern that cannot be offered by conventional tensor-

112 based analysis, thus allowing for characterizing and segmenting structural

113 subcomponents. Here we used data from two high angular resolution diffusion

114 sequences, diffusion spectrum imaging (DSI) and multi-shell imaging (MSI) and

115 examined the diffusion characteristics in the nigral and striatal efferents. We also

116   examined whether there are reliable differences in the SDFs between the GPe and the

117   GPi that allows for accurate segmentation based solely on diffusion properties. These

118   findings may identify a clear potential for using high angular resolution diffusion MRI as

119   a novel *in vivo* characterization of the microarchitecture of the human globus pallidus,

120   including the nigral and striatal efferents that break down in various neurological

121   pathologies.

122

123   **Results**

124   <u>Dorsolateral orientation of the pallidal diffusion signal</u>

125   The nigrostriatal and striatonigral fibers traverse the pallidum on the way to their targets,

126   resulting in a primarily dorsolateral-ventromedial orientation of the collective axons (Fig.

127   1A). In humans, the two segments of the pallidum are separated by a thin white matter

128   band, called the internal medullary lamina, shown in coronal sections from the Big Brain

129   atlas in Fig.1B and 1C (Amunts et al., 2013). To characterize the orientations of the

130   fibers in the inner and outer segment of the globus pallidus, we isolated the voxels

131   corresponding to the two segments (Methods, Fig 2A). Within each of these region

132   masks we estimated the SDFs from the diffusion signal of each voxel (Fig 2B-D), which

133   is a 3D representation of the underlying diffusion orientation distribution. The first three

134   peaks in each SDF were extracted and their orientation and anisotropy intensity, called

135   quantitative anisotropy (QA; Fig. 2B, see Methods), were recorded for every voxel in

136   each mask. Two representative SDFs from an example subject from the DSI dataset

6

137   show how the shapes of the SDFs differ between the inner (Fig. 2C) and outer (Fig. 2D)

138   segments of the pallidum.

139

140   Figure 3 shows the distribution of principal fiber angles across subjects in the DSI and

141   MSI samples. Each distribution was confirmed to be non-uniform using a Rayleigh's

142   test (z values > 36.12, p-values < 0.001) and exhibited consistent peaks in the

143   orientations in the fibers in both region masks and both data samples. In both the DSI

144   and MSI samples, the distribution of the angles in the inner segment is predominately

145   concentrated in the dorsolateral direction, consistent with the known orientation of the

146   major nigral and striatal efferents (Wilson 1914, Szabo 1967, Szabo 1962, Fox and

147   Rafols, 1976, Carpenter and Peter 1972). Compared to the inner segment, the

148   distribution of the angles in the outer segment is rotated medially, clockwise in the left

149   hemisphere and anticlockwise in the right hemisphere. Interestingly, this rotation is more

150   pronounced in the DSI dataset, resulting in the majority of fibers pointing dorsomedially

151   (towards the internal capsule). One possibility is that the predominantly dorsal and

152   dorsolateral fiber systems are not contributing to the strongest anisotropy pattern in the

153   DSI sample, but are still present at lower anisotropy thresholds. To explore this, we

154   looked at the orientation of the secondary fibers in both datasets (Fig. 4). Indeed, the

155   secondary fiber in the DSI dataset was oriented in a more dorsolateral direction as

156   predicted if it were reflecting the angle of the underlying nigral and striatal efferents (red

157   histogram in Fig. 4 A,B).

158

7

159   These patterns of fiber peak orientations within the SDF are also clearly visible in the

160   geometries of the extracted fibers at each voxel. Figure 5 shows a coronal slice from

161   two representative subjects from the DSI and MSI samples. A majority of the primary

162   and secondary fibers overlap in the inner segment (blue voxels) and are generally

163   oriented dorsolaterally, whereas the primary and secondary fibers in the external

164   segment (red voxels) show less overlap and exhibit a greater abundance of dorsomedial

165   orientations compared to the internal segment. Thus, the gray matter diffusion signal

166   within the pallidal nuclei has asymmetries in peak anisotropy directions that are

167   consistent with the orientation of nigral and striatal efferents running through the

168   pallidum, suggesting that the diffusion signal is sensitive to these underlying pathways.

169

170   Differential diffusion patterns between inner & outer pallidal segments

171   Along with differences in fiber orientation, we also observed general differences in the

172   sensitivity and intensity of the diffusion signal between the two pallidal segments.

173   Tensor-based analyses have shown that the anisotropy patterns around the principal

174   fiber direction tend to be highly sensitive to underlying cellular morphology differences

175   (Wiegell et al., 2003). Figure 6, panels A through D, shows the across-subject

176   probability distributions of the mean QA in the principal fiber direction, for both pallidal

177   segments. The peaks (arrows) of the distributions occurred at consistently higher

178   thresholds in the inner segment in both hemispheres and both samples. Thus, the inner

179   segment exhibited a mean shift in QA compared to the outer segment mask, suggesting

180   a slightly stronger diffusion intensity for the inner pallidal segment.

8

181

182   Differences between the pallidal segments were also reflected in the complexity of the

183   SDF geometry. The sensitivity curves in Figure 6, panels E through H, show the

184   average number of resolved fibers (y-axis) with QA values above the value shown on

185   the x-axis. Thus this measures the complexity of the diffusion geometry in each voxel by

186   showing the robustness of the fiber peaks within the reconstructed SDF across a range

187   of thresholds. As expected, the number of resolved fibers decays rapidly as the

188   threshold increases. Notably, compared to the outer segment, in the DSI sample we

189   detected more fibers in the inner segment at thresholds less than QA = 0.05 (Fig.6 E,F),

190   and more fibers in the outer segment at thresholds higher than 0.05. In the MSI sample,

191   these distributions largely overlapped (Fig.6 G,H), although the inner segment in the

192   right hemisphere showed a smaller shift in the same direction as was observed in the

193   DSI dataset. Taken together, the differences in orientation, intensity and sensitivity

194   between the structures suggest that the diffusion signal is picking up on reliable

195   differences in the cellular content of the two nuclei.

196

197   Reliable segmentation of pallidal nuclei

198   If these differences are reflecting distinctive cellular architectures and local connectivity

199   patterns then it should be possible to classify the two segments based purely on the

200   properties of the DWI signal. To this end we used k-means clustering to segment all

201   voxels within the globus pallidus using three voxel features as inputs: principle fiber

202   orientation, anisotropy of the peak fiber, and number of detected fibers. Based on these

9

203 properties alone, we generated probabilistic maps of the inner and outer segments for

204 both the DSI and MSI samples (Fig.7 A,B). Qualitative comparison of these maps shows

205 a reliable and highly similar pattern of segmentation between the two pallidal regions.

206 This is particularly evident in regions where outer and inner segments are divided along

207 a curve approximately situated on the internal medullarly lamina in both hemispheres

208 (Fig.7 A,B, and coronal slices Fig.7 D-E).

209

210 While these segmentation maps are not as clean as the hand-drawn maps based on the

211 T1 signal (Fig. 2A), the general pattern of clustering is much better than expectations

212 from chance. To explicitly quantify this, we compared the automatic segmentations to

213 the hand drawn maps against chance accuracies generated from a permutation test

214 (see Methods). Random accuracies ranged from 22% to 77% and were consistently

215 higher in the inner segment (37% to 77%) relative to the outer segment (22% to 62%)

216 reflecting the fact that there were fewer voxels within the inner segment and thus a

217 higher chance of randomly overlapping with the correct assignment. As can be seen in

218 Fig. 8, our classification significantly outperformed chance in all cases except the right

219 hemisphere of the outer segment in the MSI dataset (Fig. 8C). Furthermore, accuracies

220 were generally higher in the DSI sample than the MSI sample, likely due to the fact that

221 the DSI sample was separable along all three features included in the clustering, while

222 the MSI sample was not clearly separable based on the sensitivity curve measure (Fig.

223 6G-H).

224

10

225   <u>Consistency across data sets</u>

226   So far we have shown that both DSI and MSI samples exhibit similar differences in the

227   pallidal segment diffusion signals and similar automatic parcellations of the internal and

228   external pallidal masks. In order to quantify the similarity of the results between the two

229   samples, we correlated the voxelwise probabilities between the DSI and MSI datasets

230   (Fig. 9) for the internal and external segments separately. Overall, voxelwise

231   probabilities between the two samples were moderately correlated in both hemispheres

232   $(r(138) = 0.67$ in left hemisphere vs. $r(138) = 0.56$ in the right hemisphere), suggesting

233   that the SDF signal is capturing reliable topographic differences in underlying

234   microstructural properties that is generally consistent across samples and the type of

235   diffusion imaging approach used.

236

237   Because both the DSI and MSI samples provided similar probability profiles, we

238   aggregated both data sets to form a composite probabilistic map of the internal and

239   external pallidal segments based on the underlying diffusion structure. These merged

240   maps are shown in Figure 7C,F. Collapsing across the two acquisition methods

241   revealed an even clearer distinction between the two pallidal nuclei. This confirms that

242   classification-based purely on the properties of the diffusion signal is sufficiently robust

243   across differences in acquisition approach and scan environments to capture the major

244   divisions of the inner and outer segments of the globus pallidus.

245

246   **Discussion**

11

247 For the first time we are able to show that the orientation distribution of the diffusion

248 within the human pallidum is consistent with the presence of nigral and striatal efferents

249 that run through these nuclei. Because a large portion of these pathways is buried within

250 the pallidum, a region of high iron density, visualization of these efferents has been

251 challenging with conventional imaging approaches. If diffusion MRI proves to be a

252 reliable method of assessing the integrity of these pathways and their degradation in

253 movement disorders, then quantifying degradation within the pallidum will be necessary

254 to obtain accurate measurements of associated changes. Here we show that the SDF

255 was also able to pick up on established histological differences between the internal and

256 external segment of the globus pallidus (Hardman et al., 2002, Eid et al., 2013, Difiglia

257 and Rafols 1988), resulting in the first automatic segmentation of these two nuclei.

258 Thus, these measures are sufficiently robust to detect known differences in the pallidal

259 segments. Furthermore, these differences in the diffusion signal between the internal

260 and external segments were mostly consistent regardless of the acquisition method

261 used (i.e., DSI vs. MSI) and able to classify the separate segments with accuracies well

262 above chance expectations.

263

264 Although diffusion anisotropy measures are typically used to visualize pathways within

265 core white matter regions of the brain, here we showed that tissue characteristics

266 derived from the diffusion MRI signal, including differences in connectivity, intensity and

267 sensitivity, can distinguish nuclear properties within the pallidum itself (see also Wiegell

268 et al., 2003; Mang et al., 2012). We presume that orientations of the fibers in the two

12

269   pallidal nuclei along with differences in density and myelination contribute to the

270   characteristics of the SDFs within these voxels (Beaulieu, 2002). The predominately

271   dorsolateral orientation of the resolved fiber peaks within the pallidal segments is

272   consistent with the primary orientation of the striatopallidal, striatonigral and

273   nigrostriatal/pallidal tracts (Wilson 1914, Szabo 1967, Szabo 1962, Fox and Rafols,

274   1976, Carpenter and Peter, 1972). The more pronounced dorsolateral orientation of the

275   internal segment compared to the external segment in both the primary (Fig. 3) and

276   secondary fibers (Fig. 4) is consistent with the volumetric differences between the two

277   segments, since the nigrostriatal and striatonigral fibers traverse both segments. The

278   medial shift observed in the outer segment (Fig. 3) is likely reflecting a distinct fiber

279   system, possibly projections from the subthalamic nucleus. This open question can be

280   resolved by a direct comparison of SDFs with postmortem histological analysis, which

281   should be a goal of future work.

282

283   We should point out that the orientation of the peak fibers may not be completely

284   consistent across diffusion imaging approaches. For example, there is a more

285   pronounced medial shift in the external segment orientations in the DSI sample (Fig.3

286   A,B) than in the MSI sample (Fig.3 C,D). This may be due to the fact that the DSI

287   sample is more sensitive to underlying microarchitectural features that contribute to a

288   medial bias in the SDF signal. However, the secondary fiber in this sample was oriented

289   in a more dorsal and dorsolateral direction (Fig. 4). This suggests that these nigral and

290   striatal efferents are also present in the DSI sample, but to a weaker degree than in the

291   MSI sample. This difference is likely due to the diffusion sampling scheme used in DSI

292   and MSI. The DSI used a stronger diffusion sensitization strength (i.e. higher b-value)

293   than the MSI, and it is more sensitive to restricted diffusion in gray matter.

294

295   Being able to detect signatures of the underlying cellular content of the pallidal nuclei *in*

296   *vivo* has enormous potential as a biomarker for the integrity of basal ganglia pathways

297   and their pathology. Many movement disorders involve degradation of specific pathways

298   within the GPe and the GPi. In Parkinson's disease for example, dopaminergic neurons

299   within the substantia nigra degenerate which leads to a loss of the nigrostriatal fibers.

300   Degradation of the nigrostriatal efferents in Parkinson's patients have been recently

301   identified using diffusion MRI (Ziegler et al., 2014). Given that the nigrostriatal fibers

302   travel through the pallidum, degradation of these pathways may be reflected in the

303   integrity of the microstructural architecture exhibited by the SDFs within the pallidum.

304   Future comparative and clinical studies are needed in order to validate this assumption.

305

306   Beyond clinical implications, our results also have relevance to the investigation of basal

307   ganglia function in neurologically healthy individuals. In the canonical direct-indirect

308   pathway model of motor facilitation (Albin et al., 1989, DeLong 2000), activity in the GPe

309   is correlated with inhibiting movement initiation, through disinhibition of the sub-thalamic

310   nucleus, which in turn excites the GPi/SNr. Conversely, during movement facilitation,

311   activity within the GPi decreases. Dysfunction of the direct and indirect pathways results

312   in an imbalance between the two circuits, which causes impaired motor production as

14

313   seen in Parkinson's and Huntington's disease. If the efficiency of processing with

314   striatopallidal pathways is reflected in their microstructural integrity, then individual

315   variation in performance on tasks may be correlated with the QA distributions of the

316   striatopallidal fiber systems.

317

318   While our present results show promise for using the diffusion imaging signal as a

319   measure of cellular architecture within sub-cortical nuclei, this approach still has some

320   inherent limitations. First, as mentioned previously, diffusion imaging provides an

321   indirect measure of cellular architecture. While validation work in non-human animals

322   has provided insights into the underlying cellular properties for white matter using

323   tensor-based reconstruction approaches (Wang et al., 2011, Wang et al., 2014, Thomas

324   et al., 2014), model-based approaches have not been validated against histological

325   models, particularly in gray matter (Blumenfeld-Katzir et al., 2011). Therefore, we do

326   not know for sure what properties of the SDF reflect what properties of the underlying

327   tissue. Future studies could probe precisely how changes in SDF properties are

328   associated with variations in density, number of fibers, and myelination, by combining

329   histological analysis and diffusion imaging in animal models and post mortem tissue

330   analysis of the pallidum.

331

332   In addition, although we demonstrated that the boundaries of the pallidal nuclei are

333   resolvable based solely on diffusion information, the segmentations are imperfect. In

334   particular, there is a cluster of voxels in the anterior region of the pallidum that was

15

335   misclassified in a significant number of subjects, and the parcellations were less

336   accurate in the MSI data set as a whole. The proximity of the globus pallidus to the

337   major white matter tracts of the internal capsule may contribute to partial voluming

338   problems that contaminate the SDF signal in these voxels, resulting in classification

339   errors. Future work could adaptively cluster using more sophisticated approaches to

340   allow for noise clusters that could arise from errors in masking.

341

342   Despite this partial voluming problem, the segmentation results reported here still

343   provide evidence of robust differences between the segments of the human pallidum.

344   For example, unlike most subcortical parcellations (e.g. Behrens et al., 2003), we are

345   not supplementing the clustering features with additional distance information that adds

346   a strong prior on expected location of the nuclei. Such spatial priors would dramatically

347   clean up the underlying maps; however, the distance from the expected nuclear location

348   would become the dominant clustering feature. Although omitting these priors may lead

349   to noisier segmentations, our approach provides a more robust measure for future

350   studies to assess the pallidal cellular integrity in clinical populations.

351

352   Regardless of these limitations we have shown that the inner and outer segments of the

353   globus pallidus not only express common asymmetries in their underlying SDFs,

354   consistent with major efferent pathways, but also reliably differ among several

355   properties of the diffusion signals. This was reliable enough that a simple and automatic

356   clustering approach, based on properties of the SDF, resolved the inner and outer

16

357 segments better than chance, regardless of the imaging acquisition used (i.e., DSI or

358 MSI). This population atlas based analysis approach enables future studies to quantify

359 the extent to which microstructural variability correlates with functional properties of the

360 system, such as individual differences in inhibitory control ability and or clinical

361 pathologies of the underlying fiber systems, providing a powerful new tool for

362 investigating the cellular architecture of basal ganglia systems in vivo.

363

364 **Materials and Methods**

365 *Participants and Acquisition*

366 Two separate types of diffusion imaging were used for our analysis.

367

368 Diffusion Spectrum Imaging (DSI: CMU-60 Dataset): Twenty nine male and thirty

369 one female subjects were recruited from the local Pittsburgh community and the

370 Army Research Laboratory in Aberdeen Maryland. All subjects were

371 neurologically healthy, with no history of either head trauma or neurological or

372 psychiatric illness. Subject ages ranged from 18 to 45 years of age at the time of

373 scanning, with a mean age of 26 years (+/- 6 standard deviation). Six subjects

374 were left handed (3 males, 3 females).

375   All participants were scanned on a Siemen's Verio 3T system in the

376 Scientific Imaging & Brain Research (SIBR) Center at Carnegie Mellon University

377 using a 32-channel head coil. We collected a 50 min, 257-direction DSI scan

378 using a twice-refocused spin-echo EPI sequence and multiple q values (TR =

17

379   9,916 ms, TE = 157 ms, voxel size = 2.4mm^3, FoV = 231 x 231 mm, b-max =

380   5,000 s/mm^2, 51 slices). Head-movement was minimized during the image

381   acquisition through padding supports and all subjects were confirmed to have

382   minimal head movement during the scan prior to inclusion in the template.

383

384   Multi-shell Imaging (MSI; HCP-80 Dataset): The data were from the Human

385   connectome project at WashU-Minnesota Consortium (Q1 release). Thirty six

386   male and forty two female subjects were scanned on a customized Siemens 3T

387   "Connectome Skyra" housed at Washington University in St. Louis. Subject ages

388   ranged from 22-36 years of age at the time of scanning, with a mean age of

389   29.44 (+/- 3.5 standard deviation). All subjects were healthy, with no history of

390   neurological or psychiatric illness. The two subjects that have subsequently been

391   found by the HCP to exhibit gray matter heterotopia have been excluded from

392   this analysis. The HCP DWI session was acquired using a spin-echo EPI

393   sequence and (TR = 5520 ms, TE = 89.5 ms, voxel size = 1.25 mm^3, FoV = 210

394   x 180, 3 shells of b = 1000, 2000, 3000 s/mm^2, 111 slices, 90-directions for each

395   shell).

396

397   *Diffusion MRI Reconstruction*

398   All images were processed with a q-space diffeomorphic reconstruction method

399   described previously (Yeh and Tseng, 2011) using DSI Studio (http://dsi-

400   studio.labsolver.org/). The SDFs were reconstructed to a spatial resolution of 1 mm^3.

18

401   The white matter surface is rendered independently from an externally supplied 1 mm^3

402   resolution white matter template. The quantitative anisotropy (QA; Yeh et al., 2010) and

403   fiber orientation of the two major fibers in each voxel were exported into a separate file

404   for analysis.

405

406   *SDF Analysis*

407   Masks of the inner and outer segments of the pallidum were manually drawn by

408   identifying the internal medullarly lamina in each hemisphere on the high resolution T1

409   ICBN MNI template. In each hemisphere, the GPe was drawn by including those voxels

410   between the anterior and posterior limbs of the internal capsule, the putamen, and the

411   internal medullary lamina (outer left/right in Fig.2A). Similarly, the GPi was drawn by

412   including the voxels between the internal medullary lamina, the posterior limb and genu

413   of the internal capsule (inner left/right in Fig.2A). All region of interest masks were drawn

414   in MRICron (Rorden and Brett, 2000) and exported as NifTI images.

415

416   We then isolated the SDFs within each voxel of both region masks for analysis. For

417   illustration, Fig. 2B shows a schematized version of a SDF illustrating three resolved

418   fibers, with their independent magnitude (i.e., lengths, reflecting QA) and orientation.

419   Two representative 3D SDFs from a voxel within the left GPi and a voxel within the left

420   GPe are shown in Fig. 2 C,D. For each voxel, we took three independent measures of

421   the SDF structure: the principal fiber orientation, the number of resolved fibers across a

422   range of QA thresholds, and QA magnitude of the principal fiber. To generate the

19

423   angular distribution histograms (Figs. 3,4), we used the circstat toolbox (Berens 2009)

424   and computed the circular mean of the voxel orientations across subjects. The internal

425   capsule orientation (green arrows in Fig. 3,4) was calculated by averaging the

426   orientations across a 4mm^3 voxel cube situated prominently within the internal capsule

427   in the left and right hemispheres. For plotting purposes, a gaussian smoothing kernel

428   was applied to the QA maps (Fig. 6 A-D) for each subject (2 FWHM).

429

430   We extracted the primary fiber orientation, the number of fibers in each voxel, and the

431   QA of the primary fiber from all voxels in each mask. Then we clustered the combined

432   data across both masks using these diffusion features with a standard clustering

433   approach in Matlab (R2014a). We specified two clusters, used squared euclidean

434   distance as the distance metric and the k-means++ algorithm for cluster center

435   initialization (replicates = 10). The clusters to the inner and outer segment were

436   assigned based on the number of correctly assigned voxels relative to the hand drawn

437   masks. This algorithm generated inner and outer segment maps for each subject and

438   hemisphere in each dataset. To generate the probabilistic maps of each segment

439   across all subjects in a sample (Fig. 7), voxel probabilities were estimated by averaging

440   the binary categorization of each voxel in the inner and outer segment maps. Separate

441   probability masks were calculated for in the DSI and MSI data sets, as well as across

442   both samples (Merged). In order to quantify accuracy, we defined the classification

443   accuracy as the number of voxels correctly assigned to the inner/outer segment from

20

444   the k-means analysis using the manual segmentation as the correct assignment divided

445   by the total number of voxels in that segment (Fig. 8).

446

447   Accuracy of the clustered segments was compared against the hand-segmented region

448   of interest masks and a chance null distribution was estimated using a permutation

449   procedure. On each iteration of the permutation test, every pallidal voxel was

450   pseudorandomly assigned to either the inner or outer segment. The voxel's permuted

451   assignment was then compared to the voxel's real assignment in the manually

452   segmented pallidum masks and counted as correct if it matched that assignment. All of

453   the correct assignments were counted for each iteration of the permutation test

454   (n=1000). Chance accuracies were tallied across all iterations and the number of

455   instances that the random assignment performed better than k-means classification was

456   divided by the total number of iterations to generate the p-value for how well the

457   automated classification performs against a classification based purely on chance.

458

459   Acknowledgements

466   contained in this document are those of the authors and should not be interpreted as

467   representing the official policies, either expressed or implied, of the Army Research

468   Laboratory or the U.S. Government. The U.S. Government is authorized to reproduce

469   and distribute reprints for Government purposes notwithstanding any copyright notation

470   herein. This research was also supported in part by T32 NS007433-17.

References

471

472 Abhinav, K., Yeh, F.-C., Pathak, S., Friedlander, R. M., & Fernandez-Miranda, J. C.
473   (2014). Advanced diffusion MRI fiber tracking in neurosurgical and
474   neurodegenerative disorders and neuroanatomical studies: A review. *Biochimica et*
475   *Biophysica Acta (BBA) - Molecular Basis of Disease*.
476   doi:10.1016/j.bbadis.2014.08.002

477 Albin, R. L., Young, A. B., & Penney, J. B. (1989). The functional anatomy of basal
478   ganglia disorders. *Trends in Neurosciences*, *12*(10), 366–375. doi:10.1016/0166-
479   2236(89)90074-X

480 Alexander, G. E., DeLong, M. R., & Strick, P. L. (1986). Parallel organization of
481   functionally segregated circuits linking basal ganglia and cortex. *Annual Review of*
482   *Neuroscience*, *9*, 357–381. doi:10.1146/annurev.neuro.9.1.357

483 Amunts, K., Lepage, C., Borgeat, L., Mohlberg, H., Dickscheid, T., Rousseau, M.-É., …
484   Evans, A. C. (2013). BigBrain: an ultrahigh-resolution 3D human brain model.
485   *Science (New York, N.Y.)*, *340*(6139), 1472–5. doi:10.1126/science.1235381

486 Bastiani, M., Shah, N. J., Goebel, R., & Roebroeck, A. (2012). Human cortical
487   connectome reconstruction from diffusion weighted MRI: The effect of tractography
488   algorithm. *NeuroImage*, *62*(3), 1732–1749. doi:10.1016/j.neuroimage.2012.06.002

489 Behrens, T. E. J., Johansen-Berg, H., Woolrich, M. W., Smith, S. M., Wheeler-
490   Kingshott, C. A. M., Boulby, P. A., … Matthews, P. M. (2003). Non-invasive
491   mapping of connections between human thalamus and cortex using diffusion
492   imaging. *Nature Neuroscience*, *6*(7), 750–757.
493   doi:10.1227/01.NEU.0000309595.77090.89

494 Beaulieu, C. (2002). The basis of anisotropic water diffusion in the nervous system - A
495   technical review. *NMR in Biomedicine*. doi:10.1002/nbm.782

496 Berens, P. (2009). CircStat: A MATLAB toolbox for circular statistics. *Journal of*
497   *Statistical Software*, *31*, 1–21. doi:10.1002/wics.10

498 Beaulieu C. The basis of anisotropic water diffusion in the nervous
499 syste. NMR Biomed. 2002; 15: 435–455

500 Blumenfeld-Katzir, T., Pasternak, O., Dagan, M., & Assaf, Y. (2011). Diffusion MRI of
501   structural brain plasticity induced by a learning and memory task. *PLoS ONE*, *6*(6).
502   doi:10.1371/journal.pone.0020678
503 Burke, R. E., & O'Malley, K. (2013). Axon degeneration in Parkinson's disease.
504   *Experimental Neurology*. doi:10.1016/j.expneurol.2012.01.011

505

506 Carpenter, M. B., & Peter, P. (1972). Nigrostriatal and nigrothalamic fibers in the rhesus
507   monkey. *The Journal of Comparative Neurology*, *144*(1), 93–115.
508   doi:10.1002/cne.901440105

509 Carpenter, M. B., & Mcmasters, R. E. (1964). Lesions of the Substantia Nigra in the
510   Rhesus Monkey. Efferent Fiber Degeneration and Behavioral Observations. *The*
511   *American Journal of Anatomy*, *114*, 293–319.

512 Cossette, M., Lévesque, M., & Parent, A. (1999). Extrastriatal dopaminergic innervation
513 of human basal ganglia. *Neuroscience Research*, *34*(1), 51–54.

514 DeLong, M. R. (1990). Primate models of movement disorders of basal ganglia origin.
515   *Trends in Neurosciences*, *13*(7), 281–285. doi:10.1016/0166-2236(90)90110-V

516 Difiglia, M., & Rafols, J. A. (1988). Synaptic organization of the globus pallidus. *Journal*
517   *of Electron Microscopy Technique*, *10*(3), 247–263. doi:10.1002/jemt.1060100304

518 Eid, L., Champigny, M. F., Parent, A., & Parent, M. (2013). Quantitative and
519   ultrastructural study of serotonin innervation of the globus pallidus in squirrel
520   monkeys. *European Journal of Neuroscience*, *37*(10), 1659–1668.
521   doi:10.1111/ejn.12164

522 Fernández-Miranda, J. C., Wang, Y., Pathak, S., Stefaneau, L., Verstynen, T., & Yeh, F.
523   C. (2014). Asymmetry, connectivity, and segmentation of the arcuate fascicle in the
524   human brain. *Brain Structure and Function*. doi:10.1007/s00429-014-0751-7

525 Fox, C. A., & Rafols, J. A. (1976). The striatal efferents in the globus pallidus and in the
526   substantia nigra. *Research Publications - Association for Research in Nervous and*
527   *Mental Disease*, *55*, 37–55.

528 Haber, S. N., Fudge, J. L., & McFarland, N. R. (2000). Striatonigrostriatal pathways in
529   primates form an ascending spiral from the shell to the dorsolateral striatum. *The*
530   *Journal of Neuroscience : The Official Journal of the Society for Neuroscience*,
531   *20*(6), 2369–2382. doi:http://www.jneurosci.org/content/20/6/2369

532 Haber, S. N. (2003). The primate basal ganglia: Parallel and integrative networks. In
533   *Journal of Chemical Neuroanatomy* (Vol. 26, pp. 317–330).
534   doi:10.1016/j.jchemneu.2003.10.003

535 Hardman, C. D., Henderson, J. M., Finkelstein, D. I., Horne, M. K., Paxinos, G., &
536   Halliday, G. M. (2002). Comparison of the basal ganglia in rats, marmosets,
537   macaques, baboons, and humans: Volume and neuronal number for the output,
538   internal relay, and striatal modulating nuclei. *Journal of Comparative Neurology*,
539   *445*(3), 238–255. doi:10.1002/cne.10165

24

540 Hollerman, J. R., Tremblay, L., & Schultz, W. (2000). Involvement of basal ganglia and
541   orbitofrontal cortex in goal-directed behavior. In *Progress in Brain Research* (Vol.
542   126, pp. 193–215). doi:10.1016/S0079-6123(00)26015-9

543 Mang, S. C., Busza, A., Reiterer, S., Grodd, W., & Klose, A. U. (2012). Thalamus
544   segmentation based on the local diffusion direction: A group study. *Magnetic*
545   *Resonance in Medicine*, *67*(1), 118–126. doi:10.1002/mrm.22996

546 Reiner, A., Albin, R. L., Anderson, K. D., D'Amato, C. J., Penney, J. B., & Young, A. B.
547   (1988). Differential loss of striatal projection neurons in Huntington disease.
548   *Proceedings of the National Academy of Sciences of the United States of America*,
549   *85*(15), 5733–5737. doi:10.1073/pnas.85.15.5733

550 Rorden, C., & Brett, M. (2000). Stereotaxic display of brain lesions. *Behavioural*
551 *Neurology*, *12*(4), 191–200.

552 Szabo, J. (1967). The efferent projections of the putamen in the monkey. *Experimental*
553   *Neurology*, *19*(4), 463–476. doi:10.1016/0014-4886(67)90166-5

554 Szabo, J. (1962). Topical distribution of the striatal efferents in the monkey.
555   *Experimental Neurology*, *5*(1), 21–36. doi:10.1016/0014-4886(62)90067-5

556 Thomas, C., Ye, F. Q., Irfanoglu, M. O., Modi, P., Saleem, K. S., Leopold, D. A., &
557   Pierpaoli, C. (2014). Anatomical accuracy of brain connections derived from
558   diffusion MRI tractography is inherently limited. *Proceedings of the National*
559   *Academy of Sciences*, *111*(46), 16574–16579. doi:10.1073/pnas.1405672111

560 Wang, Y., Fernández-Miranda, J. C., Verstynen, T., Pathak, S., Schneider, W., & Yeh,
561   F. C. (2013). Rethinking the role of the middle longitudinal fascicle in language and
562   auditory pathways. *Cerebral Cortex*, *23*(10), 2347–2356.
563   doi:10.1093/cercor/bhs225

564 Wang, Y., Wang, Q., Haldar, J. P., Yeh, F. C., Xie, M., Sun, P., … Song, S. K. (2011).
565   Quantification of increased cellularity during inflammatory demyelination. In *Brain*
566   (Vol. 134, pp. 3587–3598). doi:10.1093/brain/awr307

567 Wang, X., Cusick, M. F., Wang, Y., Sun, P., Libbey, J. E., Trinkaus, K., … Song, S. K.
568   (2014). Diffusion basis spectrum imaging detects and distinguishes coexisting
569   subclinical inflammation, demyelination and axonal injury in experimental
570   autoimmune encephalomyelitis mice. *NMR in Biomedicine*, *27*(7), 843–852.
571   doi:10.1002/nbm.3129

572 Wedeen, V. J., Wang, R. P., Schmahmann, J. D., Benner, T., Tseng, W. Y. I., Dai, G.,
573   … de Crespigny, A. J. (2008). Diffusion spectrum magnetic resonance imaging
574   (DSI) tractography of crossing fibers. *NeuroImage*, *41*(4), 1267–1277.
575   doi:10.1016/j.neuroimage.2008.03.036

576 Wiegell, M. R., Tuch, D. S., Larsson, H. B., & Wedeen, V. J. (2003). Automatic
577   segmentation of thalamic nuclei from diffusion tensor magnetic resonance imaging.
578   *Neuroimage*, *19*(2 Pt 1), 391–401. doi:10.1016/S1053-8119(03)00044-2

579 Wilson, S. a K. (1914). An experimental research into the anatomy and physiology of
580   the corpus striatum. *Brain*, *36*, 427–492.

581 Yeh, F. C., & Tseng, W. Y. I. (2011). NTU-90: A high angular resolution brain atlas
582   constructed by q-space diffeomorphic reconstruction. *NeuroImage*, *58*(1), 91–99.
583   doi:10.1016/j.neuroimage.2011.06.021

584 Yeh, F. C., Wedeen, V. J., & Tseng, W. Y. I. (2010). Generalized q-sampling imaging.
585   *IEEE Transactions on Medical Imaging*, *29*(9), 1626–1635.
586   doi:10.1109/TMI.2010.2045126

587 Ziegler, E., Rouillard, M., André, E., Coolen, T., Stender, J., Balteau, E., … Garraux, G.
588   (2014). Mapping track density changes in nigrostriatal and extranigral pathways in
589   Parkinson's disease. *NeuroImage*, *99*, 498–508.
590   doi:10.1016/j.neuroimage.2014.06.033

591

592

593

594

595

596

597

598

599

600

601
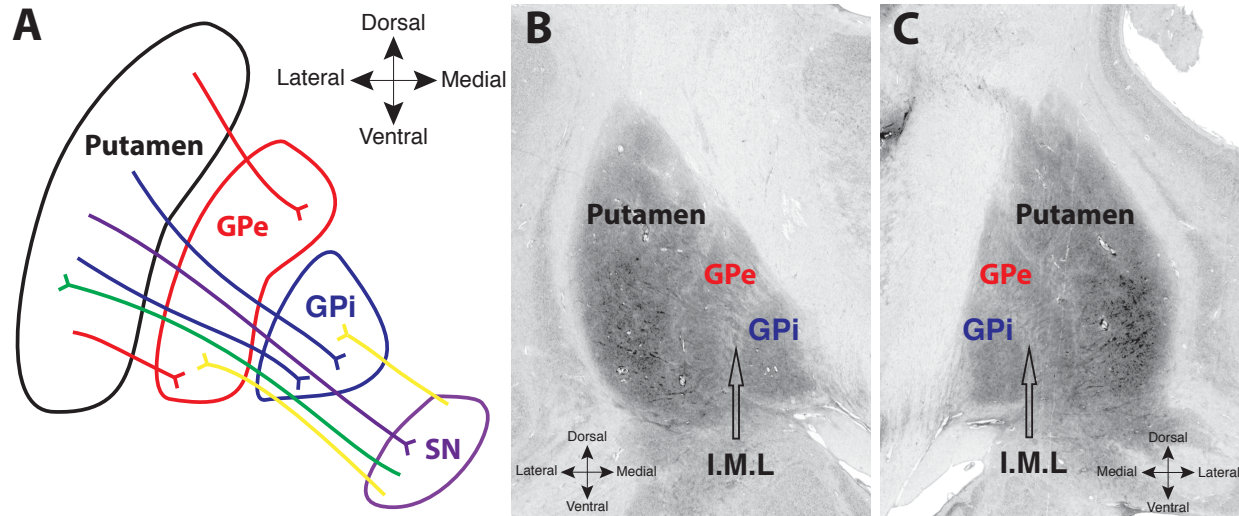
Fig. 1

A. Schematic of fiber systems traversing the internal (GPi) and external (GPe) segments of the pallidum, including projections to and from the substantia nigra. Labeled pathways include nigrostriatal (green) striatopallidal (red, cyan), striatalnigral (purple) and nigropallidal (yellow (red, blue), striatonigral (purple) and nigropallidal (yellow). B and C. Coronal images from the Big Brain atlas, showing the putamen, GPe, and GPi, in the left (B) and right (C) hemispheres; black arrows point to the approximate center of the internal medullary lamina (I.M.L) separating the two segments (slice 3894, Amunts 2013).
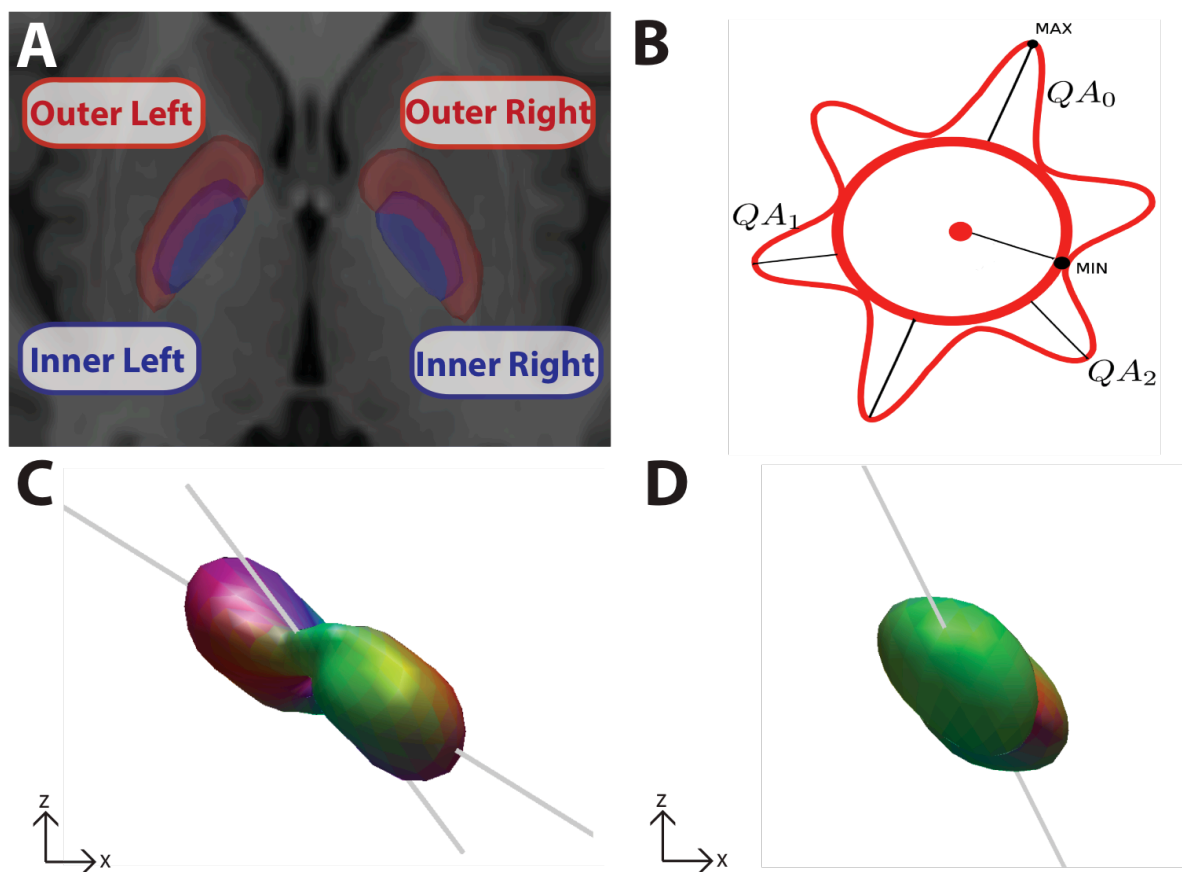
Fig. 2
A. The inner (blue) and outer (red) segments of the left and right pallidum were manually drawn on the high resolution T1 ICBM 152 template. B. Schematized version of an SDF illustrating three resolved fibers (QA0, QA1, QA2), their magnitude (i.e., lengths, reflecting QA) and orientation. C,D Representative SDFs from the left internal segment (C) and left external segment (D) in the coronal plane from a single subject from the DSI dataset. Gray lines indicate direction of fiber orientations.

Primary Fiber
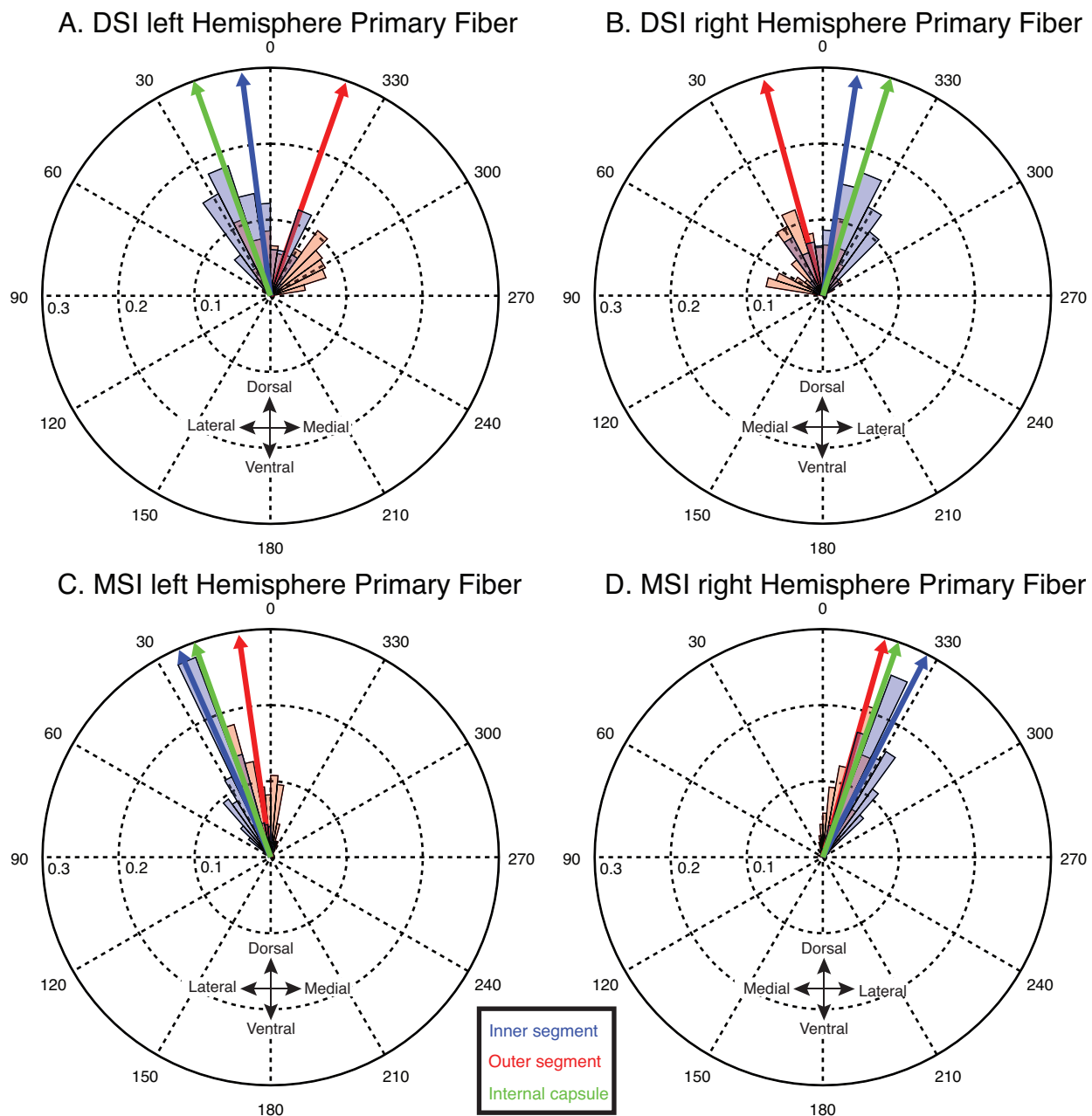
620
621
622   Fig. 3
623   Angular distributions of primary fibers from DSI (A,C) and MSI (C,D) datasets. Blue,
624   red, and green arrows indicate the mean of the distributions in the inner, outer and
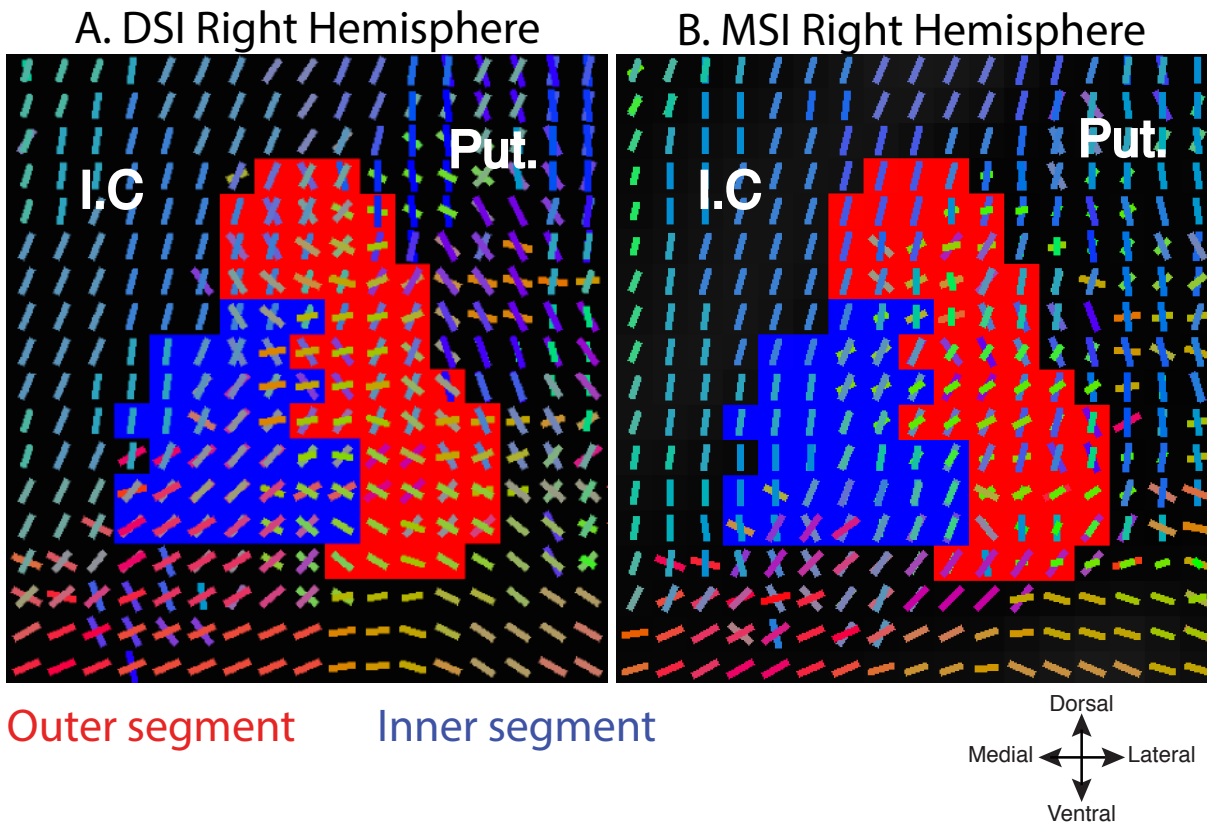625   internal capsule respectively.

Secondary Fiber
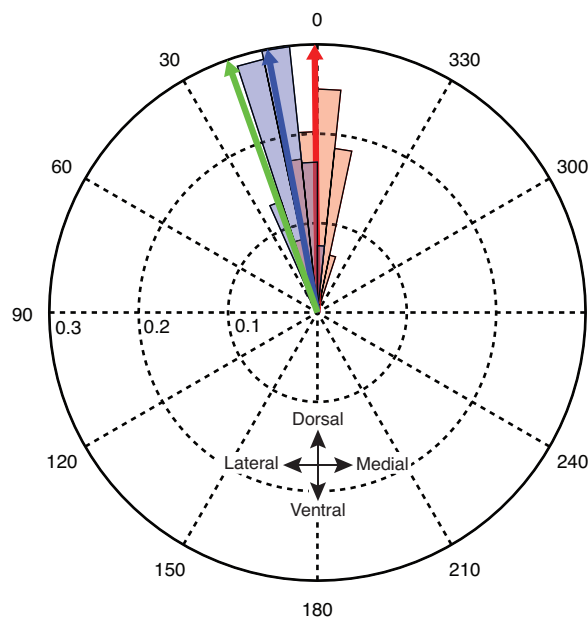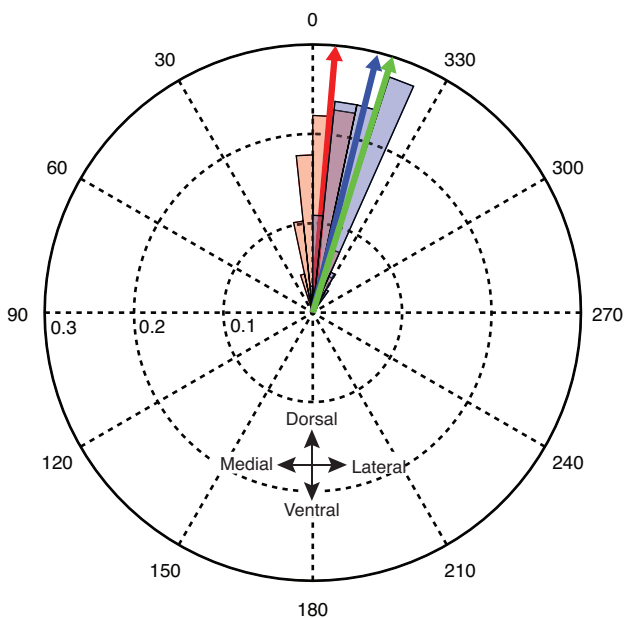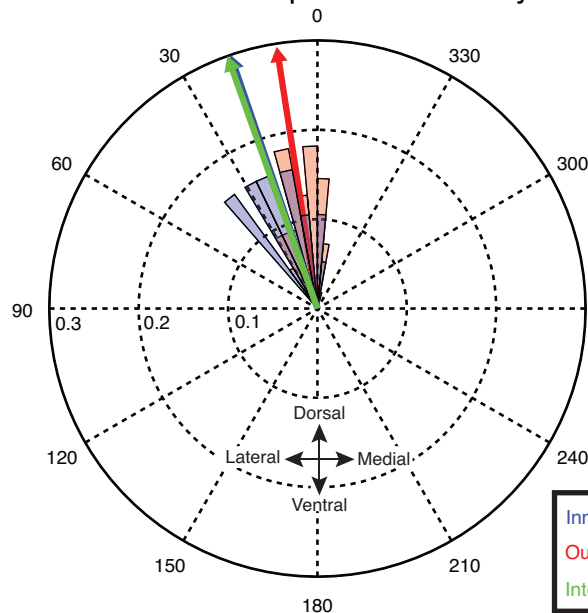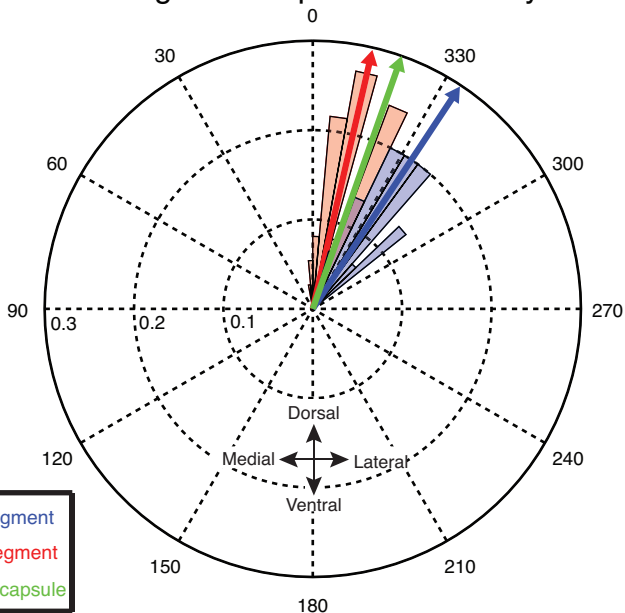
626
627 Fig. 4
628 Angular distributions of secondary fibers from DSI (A,C) and MSI (C,D) datasets. Blue,
629 red, and green arrows indicate the mean of the distributions in the inner, outer and
630 internal capsule respectively.

30

Fig. 5
Voxelwise geometries of the primary and secondary fibers, inner (blue) and outer (red), segments of two example subjects from the DSI (A) and MSI (B) datasets. Slices are both from y = -1 (MNI). (Putamen (Put.), Internal capsule (I.C.). Fiber orientations are color coded according to their orientation.
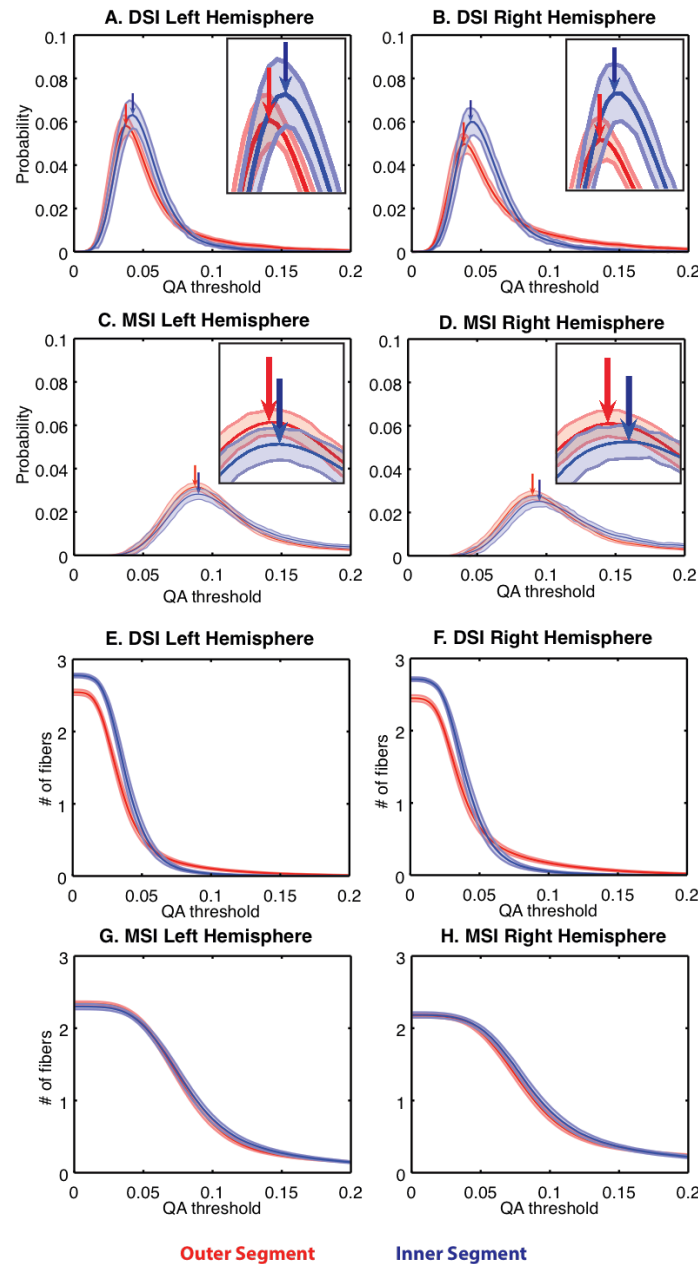
637
638
639   Fig. 6
640   A-D. Probability density functions of the primary fiber QA of the inner (blue) and outer
641   (red) segments in the DSI(A,B) and MSI(C,D) datasets. E-H The number of resolved
642   fibers thresholded by QA in the inner and outer segments in the DSI (A,B) and MSI
643   datasets (C,D). Arrows indicate peaks of the distributions. Lines indicate mean and
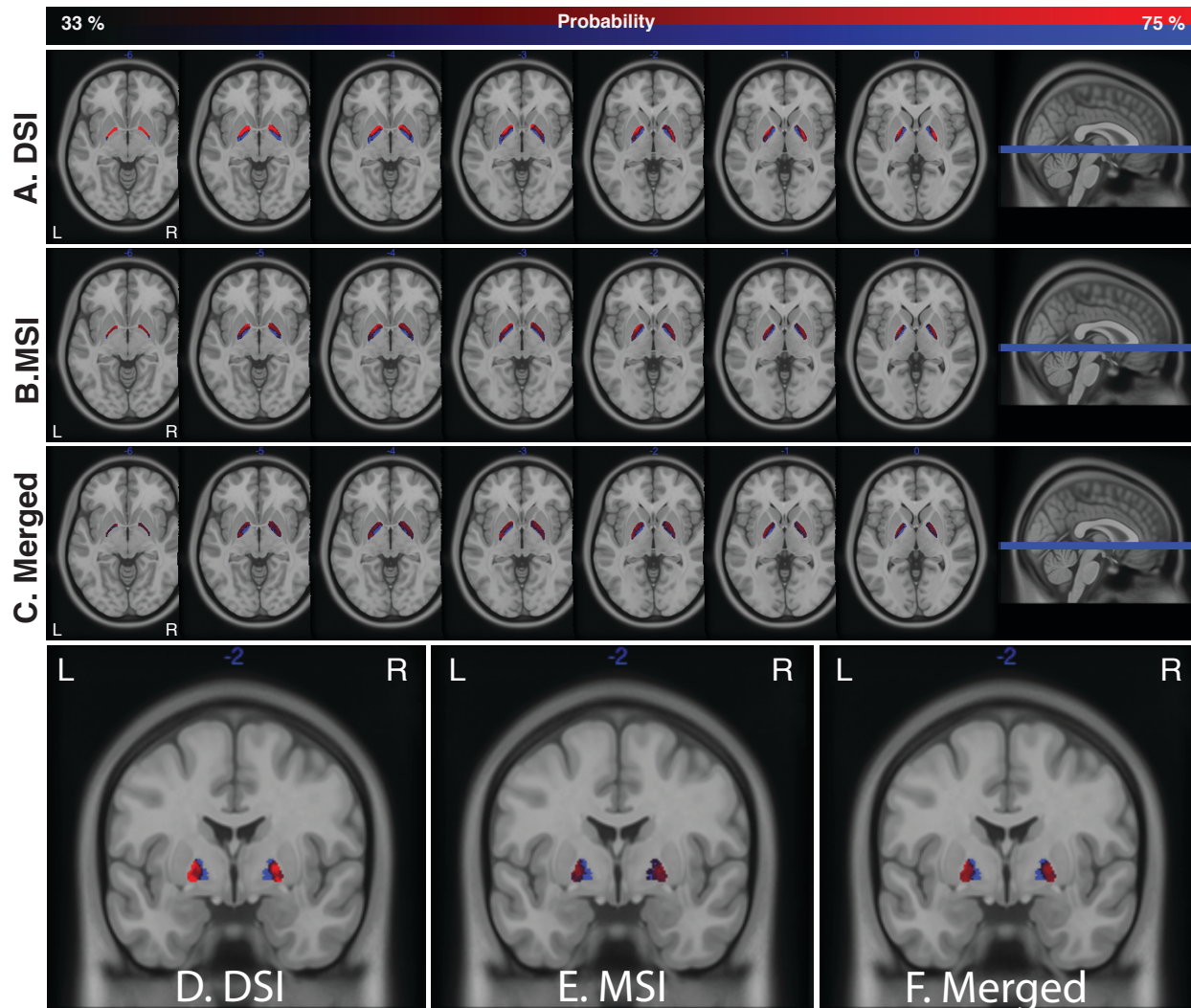644   shaded regions are 95% confidence intervals.

32

Fig. 7

A-C. Probabilistic maps, across subjects, of the inner and outer segments in the DSI (A), MSI (B), and merged (C) datasets. Maps are thresholded between 33-77% probability. The background image in each image is the T1 ICBM template. Axial images span z coordinates [-6,0]. D-F. Coronal images of the same probabilistic maps at y = -2.

653
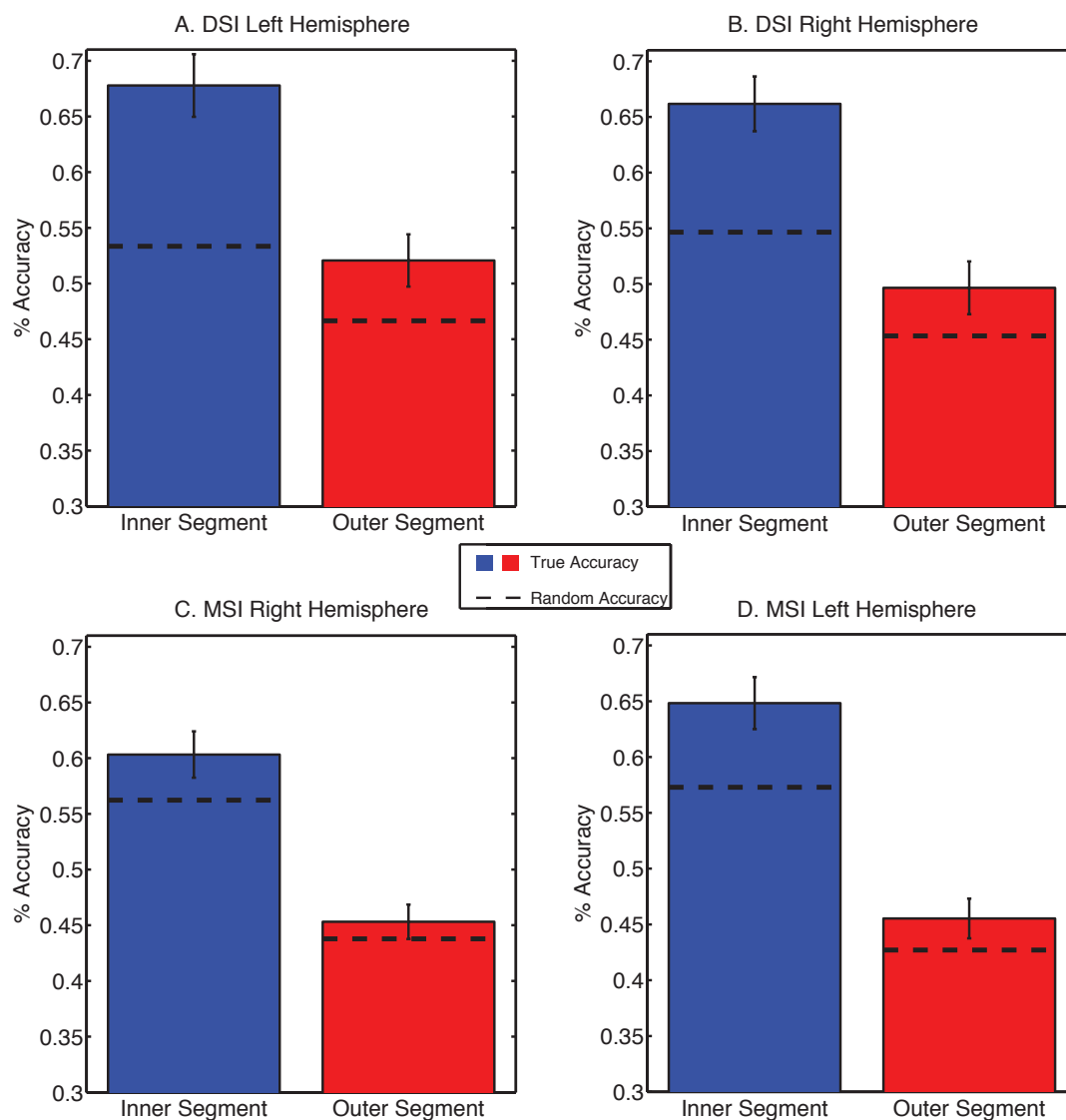654 Fig. 8
655 A-D. Mean accuracy results from k-means classification in the DSI (A,B) and MSI (C,D)
656 datasets. Dotted lines show random accuracies obtained from 1000 iterations of a
657 permutation test where clustered categories were scrambled. Error bars indicate 95%
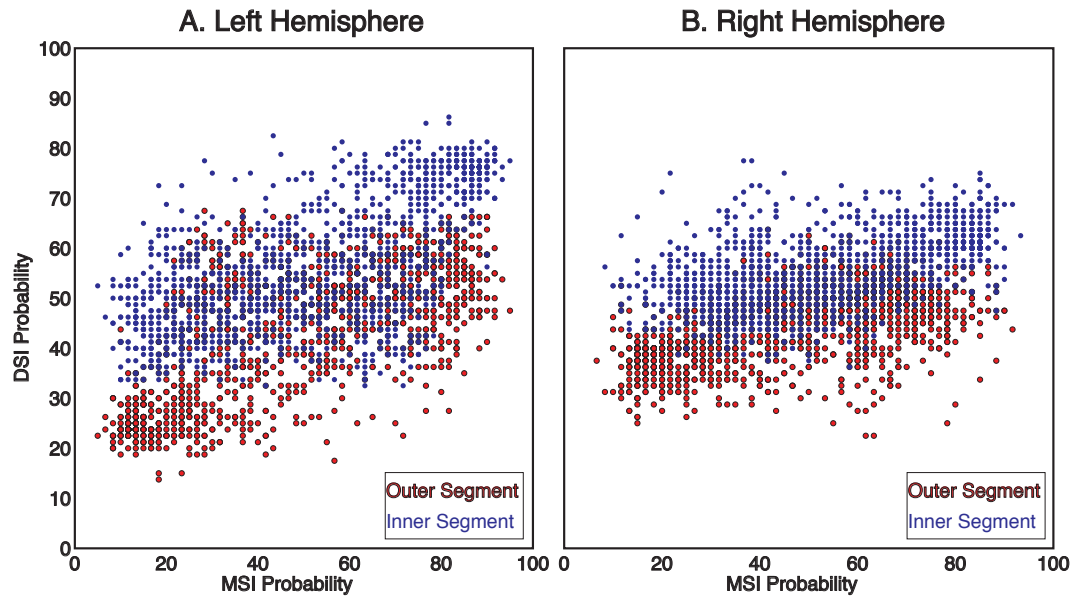658 confidence intervals across subjects.

659
660 Fig. 9
661 The voxelwise MSI probability (averaged across individual subjects) plotted against
662 voxelwise DSI probability for each voxel in the left (A) and right (B) hemispheres. Each
663 point corresponds to an individual voxel in either the outer (red) or inner (blue) segment.